International Astronautical Congress, Antalya, Türkiye, 5-9 October 2026.

IAC-26-A5-IPB-14-x107030

Diana: A Satellite-Based Lunar Time and Frequency System

Changgang Zheng[a b]*, **Luyuan Wang**[a], **Jionghui Li**[a], **Haonan Li**[c], **Zihao Fan**[d], **Mingxin Li**[b], **Bo Jiang**[d], **Tian Pan**[c], **Jinjun Zheng**[e]

[a] *Institute of Spacecraft System Engineering, Beijing, China*
[b] *Nanjing University, Nanjing, China*
[c] *Beijing University of Posts and Telecommunications, Beijing, China*
[d] *Shanghai Jiao Tong University, Shanghai, China*
[e] *Institute of Telecommunication and Navigation Satellites, Beijing, China*

* Corresponding Author

Abstract

Continuous and high-precision time and frequency synchronization is a fundamental enabler for lunar exploration and sustained surface operations, supporting navigation, communication, and scientific systems. However, existing lunar time references (time and frequency) remain heavily dependent on Earth-based UTC. Long propagation delays, intermittent Earth–Moon visibility, and link instability prevent time from being maintained as a continuously available system resource for lunar infrastructures. As an alternative to Earth-dependent time references, lunar-surface-based timekeeping is severely constrained by prolonged lunar nights, extreme thermal conditions, limited energy availability, and the absence of robust, wide-area time and frequency dissemination mechanisms. The absence of an autonomous lunar time and frequency standard thus leads to fundamental system-level limitations, including unstable lunar PNT solutions, reduced communication capacity, and impaired coordination among distributed lunar assets, particularly for farside and long-duration missions. This paper proposes Diana, an autonomous satellite system in lunar orbit for generating and disseminating lunar standard time and frequency, as infrastructure to support human exploration of the Moon. Diana is built upon a dual-plane distant retrograde orbit (DRO) constellation with right ascension separation, enabling continuous full-lunar coverage. The architecture integrates multi-state & multi-frequency transceivers, an ALGOS-based ensemble timekeeping algorithm combined with Kalman plus weights, a pulsar-based time calibration mechanism, and an Earth time comparison module. The proposed system enables the autonomous generation, long-term stabilization, and full lunar coverage dissemination of lunar standard time and frequency. Performance analysis shows a long-term frequency stability of 1×10^{-15} per day, two-way time-transfer accuracy better than 0.2 ns, and absolute time accuracy better than 100 ns. Time comparison errors with Earth-based BDT and UTC are maintained within 0.5 ns and 10 ns, respectively. These results demonstrate that Diana provides a feasible and scalable foundation for future lunar navigation, communication, and sustainable lunar infrastructure. Diana is designed as an open architecture that enables international participation, allowing independently operated timekeeping satellites to be integrated into the constellation and jointly contribute to a federated lunar timekeeping ensemble.

Keywords: Lunar Standard Time and Frequency; Satellite Timekeeping; Time and Frequency Transfer; Atomic Clock Ensemble; Lunar PNT

1. Introduction

The time and frequency references used by current lunar spacecraft remain highly dependent on Earth-based UTC. This dependence leads to limited autonomy, poor continuity, large synchronization errors, and vulnerability of the Earth–Moon link to disruptions [1, 2]. A continuously operating local timekeeping system is also difficult to establish on the lunar surface because of the long and extremely cold lunar night [3–7]. Even if permanent research stations and high-precision atomic time and frequency sources are deployed on the Moon in the near future, the number of permanently operating surface facilities will remain very limited. A surface-only architecture would therefore be unable to provide a physical time-frequency reference covering the whole Moon, or to provide convenient high-precision timing service to users at arbitrary lunar locations. In addition, present calibration methods rely mainly on Earth. This creates engineering compatibility constraints and introduces measurement errors over the very long Earth–Moon distance, so the accuracy of lunar time remains lower than that of terrestrial time.

As lunar activities increase worldwide, the establishment of a unified lunar time system has become a major topic, especially in the context of the U.S. return to the Moon [8, 9], ESA's Moonlight programme [10], and China's International Lunar Research Station [11, 12].

In April 2024, the White House Office of Science and Technology Policy requested NASA to lead the formulation of an implementation plan for coordinated lunar time [13]. NASA tends to consider an independent lunar time scale that remains traceable to UTC. One concept is to form a lunar master clock, analogous to UTC on Earth, by weighted averaging of atomic clocks on the lunar surface or in lunar orbit. The specific clock-station locations, algorithms, and implementation modes are still under study.

Europe places greater emphasis on the international co-definition of lunar standard time [14]. ESA often uses the concept of lunar reference time, and has maintained technical openness between an independent lunar time scale and an Earth-synchronized time. Recent discussions tend toward an independent time scale that runs naturally in the lunar gravitational environment, with preference for a selenocentric coordinate time defined by the International Astronomical Union.

Chinese researchers have proposed three technical routes for lunar standard time [15]. The first is to directly adopt selenocentric coordinate time. The second is to establish a lunar-surface time consistent with the mean rate of atomic clocks on the lunar geoid. The third is to establish an adjusted coordinated time that retains only periodic differences with Earth time. No consensus has yet been reached.

The international differences do not mainly concern the definition of the second; they concern the reference origin and the naming of international standards.

This paper does not attempt to resolve these differences. Instead, it focuses on how to physically establish the required lunar standard time in lunar orbit. By specifying the clock-station orbit, timekeeping algorithm, and implementation method, this paper proposes an autonomous, high-precision, relativistically consistent method for generating and disseminating lunar standard time and frequency. The method addresses the low autonomy and continuity, limited accuracy, single calibration source, insufficient coverage, and compatibility limitations of current lunar time-frequency references. A satellite-based system is used to form a local dynamic lunar timekeeping ensemble, generate the time-frequency reference autonomously, and reduce dependence on Earth links. Pulsar time is introduced as a core calibration source to improve long-term stability. Considering the importance of UTC, Earth–Moon measurement links are used only for offset comparison, thereby satisfying terrestrial reference-comparison requirements while preserving the autonomy of lunar time. The Earth–Moon measurement link is also made compatible with the BeiDou system [16, 17] to improve engineering feasibility. Finally, the lunar coverage of satellites carrying lunar standard time enables unobstructed timing service over the entire lunar surface.

2. Basic Principle

The proposed method uses a dual-plane distant retrograde orbit (DRO) constellation around the Moon, specifically comprising high-altitude retrograde lunar orbits. It combines a three-state multi-frequency satellite transceiver design, an ALGOS-based ensemble timekeeping algorithm [18, 19] integrated with weighted Kalman filtering [20], and a cooperative scheme of pulsar-time calibration and Earth-time comparison. The objective is to autonomously generate, stably maintain, and disseminate lunar standard time and frequency (LSTF) over the entire Moon.

2.1 Constellation Configuration

The satellite system consists of two adjacent DROs. The two orbits have the same shape in the lunar inertial frame, and all orbital-plane parameters are identical except for the right ascension of the ascending node (RAAN). The RAAN separation is $\Delta\Omega$. Inter-satellite measurement and data-transfer links connect all satellites into a space-based joint timekeeping laboratory. In the initial deployment, the number of satellites is small and the inter-satellite distance is kept as short as possible, forming a compact DNA-like configuration. As the number of satellites increases, the constellation expands toward both ends and finally forms a complete ring, as illustrated in Fig. 1.

The satellite parameters on each orbit are selected under the following constraints in the lunar inertial frame.

(C1) For an orbital semi-major axis a_{sat}, lunar mean radius R_m, and minimum user elevation angle E, full lunar coverage imposes an upper bound on the orbital inclination. For the retrograde orbit considered here, with i in the range of $140°$–$180°$, the maximum allowable inclination is given

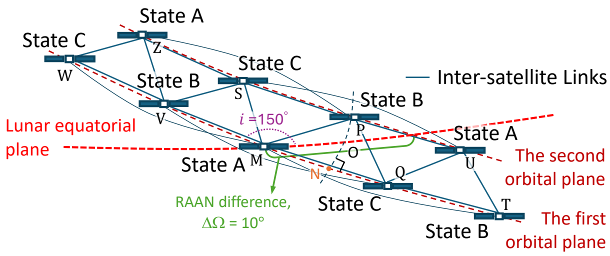

Fig. 1: Schematic constellation configuration.

by

$$i_{\max} = \pi - \arcsin\left[\frac{R_m \sin(\pi/2 + E)}{a_{sat}}\right] - E. \tag{1}$$

Accordingly, the orbital inclination should satisfy $i \le i_{\max}$.

(C2) The first DRO satellite in orbital plane X is defined as the reference satellite. If the phase of the reference satellite is zero, subsequent satellites are placed sequentially at phases α, $-\alpha$, 2α, -2α, and so on. Satellites in orbital plane Y are placed in the same way. The phase separation angle is

$$\alpha = 2\arctan\left[\cos(\pi - i)\tan\left(\frac{\Delta\Omega}{2}\right)\right]. \tag{2}$$

(C3) At the initial epoch, the true anomalies of the reference satellites in planes X and Y differ by $\alpha/2$, so that the minimum distance between the two reference satellites over one orbital period is minimized. The angle between the two orbital planes is

$$\beta = 2\arcsin\left[\sin\left(\frac{\Delta\Omega}{2}\right)\sin(\pi - i)\right]. \tag{3}$$

(C4) Let the DRO orbital period be T_s and the lunar rotation period be T_m. To ensure that a lunar-surface user can conduct at least one time-frequency comparison within $T_m/2$, the orbital period must satisfy

$$\begin{aligned} \gamma &= \frac{\pi}{2} - E - \arcsin\left[\frac{R_m}{a_{sat}}\sin\left(\frac{\pi}{2} + E\right)\right], \\ \frac{2\pi T_s}{T_m} &< 2\arcsin\left[\frac{\sin\gamma}{\sin(\pi - i)}\right]. \end{aligned} \tag{4}$$

During deployment, the reference satellite in plane X is deployed first, followed by the reference satellite in plane Y. Subsequent satellites are deployed alternately in the two planes. If multiple satellites are launched by a single launch vehicle, the deployment sequence may be adjusted as long as the final multi-satellite state satisfies the design.

The reference satellite in plane X establishes inter-satellite links with the two nearest satellites on the left and the two nearest satellites on the right in the same orbit. It also links with the reference satellite in plane Y and one adjacent satellite in plane Y. The inter-satellite antenna beam coverage is designed to support six simultaneous links.

The maximum inter-plane link distance is the link between the reference satellites in planes X and Y. The maximum inter-satellite distance is given by

$$R_{maxXY} = 2a_{sat}\sin\left\{0.5\arccos\left[\cos(0.5\alpha)\cos(\beta)\right]\right\}. \tag{5}$$

The maximum distance between satellites in the same orbital plane is

$$R_{maxXX} \; or \; R_{maxYY} = 2a_{sat}\sin(\alpha). \tag{6}$$

The adjacent satellite in plane Y is selected as the one closer to the reference satellite in plane X. Its maximum inter-satellite distance is

$$\begin{aligned} C_{XYn} &= \cos(\alpha)\cos(\beta) + \sin(\alpha)\sin(\beta) \\ &\quad \times \cos\left[\frac{\pi}{2} - \arcsin\left(\frac{\sin(0.5\alpha)}{\sin\beta}\right)\right], \\ R_{maxXYn} &= 2a_{sat}\sin\left[0.5\arccos(C_{XYn})\right]. \end{aligned} \tag{7}$$

The maximum value calculated from Eqs. (5)–(7) is used as the minimum inter-satellite link range required within the constellation. This range determines the transmit EIRP and receive G/T of the inter-satellite link equipment.

The minimum inter-satellite link distance occurs when a satellite in plane Y reaches the intersection with plane X and is closest to a satellite in plane X. It is

$$R_{min} = 2a_{sat}\sin(\alpha/4). \tag{8}$$

The inter-satellite link uses full-duplex continuous measurement. The constellation uses three frequency states. A state-A satellite transmits f_a and receives f_b and f_c; a state-B satellite transmits f_b and receives f_a and f_c; and a state-C satellite transmits f_c and receives f_a and f_b. Satellites in different states can establish inter-satellite links.

The transmit frequency is phase-locked to the satellite reference time and frequency, supporting two-way carrier-phase measurement for time comparison. Following international standards or common practice for lunar-orbit frequency allocation, f_a, f_b, and f_c may be selected from the 2483–2500 MHz, 2200–2290 MHz, and 2025–2110 MHz bands, respectively. The mapping between states and frequency bands may be exchanged and need not be fixed.

If a satellite in an orbital plane is in state A, its immediate left-hand neighbor in the same orbit is in state B and its immediate right-hand neighbor is in state C. If it is in state B, the left-hand neighbor is in state C and the right-hand neighbor is in state A. If it is in state C, the left-hand neighbor is in state A and the right-hand neighbor is in state B.

If the reference satellite in plane X is in state A, the reference satellite in plane Y is in state B. If the reference satellite in plane X is in state B, the reference satellite in plane Y is in state C. If the reference satellite in plane X is in state C, the reference satellite in plane Y is in state A.

A specific constellation design uses nine satellites in circular DROs with a semi-major axis of 10238 km and an inclination of $150°$. The orbital period is about 25.8 h. The satellites are distributed in two orbital planes with a RAAN separation of $10°$: five satellites in the first plane and four in the second plane.

The satellites operate on circular orbits at the same altitude. When two satellites are at their nearest distance, the off-axis angle of the inter-satellite-link antenna, where the direction from the satellite to the lunar center is defined as $0°$, is largest. When they are at their farthest distance, the off-axis angle is smallest. The antenna coverage range is shown in Fig. 2, where $\theta_{min} = 2.17°$ and $\theta_{max} = 8.7°$. This angle is the complement of the off-axis angle. The minimum inter-satellite antenna coverage is $360°$ in azimuth, with elevation from θ_{min} to θ_{max}.

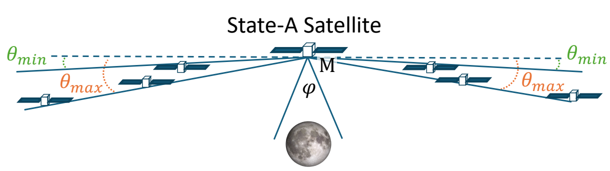

Fig. 2: Beam angles of the inter-satellite-link antenna and lunar-facing antenna for a state-A satellite.

To establish as many simultaneous inter-satellite links as possible, four inter-satellite-link antennas are installed in four directions. Each antenna covers one azimuth quadrant. The half-power beamwidth is $90°$ in azimuth and $10°$ in elevation, with a downward installation angle of $5°$. With an efficiency of 0.7, each antenna has a gain of about 14 dBi. A 10 W solid-state power amplifier is divided into four outputs for the four antennas. Considering an additional 3 dB loss, the transmitted EIRP of each antenna is about 16 dBW. With a maximum path loss of 169.5 dB, antenna reciprocity gives a receive antenna gain of about 14 dBi. The receiver G/T is about -16 dB/K, and the received carrier-to-noise-density ratio is about 59 dB-Hz.

Inter-satellite data transmission uses UQPSK modulation and LDPC coding. The I branch is the measurement branch with a data rate of 1000 bps, and the Q branch is the communication branch with a data rate of 5000 bps. The power ratio between the two branches is 1:5, and the demodulation margin is greater than 13 dB. Code-division multiple access is used with a spreading-code rate of 10.23 Mcps. The I-branch code period is 10230 chips, and the Q-branch code period is 2046 chips. The near-far effect caused by different inter-satellite ranges keeps the power difference between strong and weak signals within 7 dB, so it does not trigger a correlation false-decision threshold.

2.2 *Generation of Lunar Standard Time and Frequency*

All satellites carry atomic clocks for timekeeping, and some satellites carry reference clocks. The onboard atomic-clock model accounts for the lunar-centered inertial gravitational field, relative motion, onboard temperature drift, magnetic-field variation, and other environmental factors. Relativistic correction terms, including lunar gravitational frequency shift, are included. The clock model is reduced to the lunar barycenter and describes the characteristics of selenocentric coordinate time.

The onboard timekeeping clocks and reference clocks form a static-dynamic constellation clock ensemble through onboard time-frequency comparison links and inter-satellite time-frequency comparison links. The constellation clock ensemble uses ALGOS and weighted Kalman filtering for integrated timekeeping.

- Prior Allan variance and Hadamard variance are used to estimate the current stability of each atomic clock in the ensemble, providing a basis for weight adjustment.
- The weights, process-noise covariance, and observation-noise covariance are determined from the clock stability indicators. A weighted Kalman filter generates the paper master-clock signal of the constellation ensemble to ensure high precision and high stability.
- The timekeeping algorithm computes, in real time, the time-frequency offset parameters between the master-clock signal and each atomic clock in the ensemble. These parameters are sent periodically to the satellite carrying each atomic clock through onboard and inter-satellite links. The specific period is determined by the performance of each atomic clock.
- Each satellite uses the time-frequency offset parameters to align its reference time and frequency with the

paper master clock, without steering the free-running onboard atomic clock.

- Comparisons between satellite reference time-frequency signals are completed through inter-satellite links. The comparison result $\Delta t_{i,j}$ between the reference time-frequency of satellite i and that of satellite j is shared across the constellation. The comparison result $\Delta t^{i,m}$ between the reference time-frequency of satellite i and onboard atomic clock m is obtained through the onboard comparison link and shared with other satellites. Similarly, the comparison result $\Delta t^{j,n}$ between satellite j and onboard atomic clock n is shared through inter-satellite links.

- Using $\Delta t^{i,m}$, $\Delta t^{j,n}$, and $\Delta t_{i,j}$, the comparison between the mth atomic clock on satellite i and the nth atomic clock on satellite j is obtained as

$$\Delta\tau^{i,m}_{j,n} = \Delta t^{i,m} - \Delta t_{i,j} - \Delta t^{j,n}. \tag{9}$$

- After outlier removal, all pairwise clock-difference data from the working atomic clocks in the constellation are input to the ALGOS and weighted Kalman filtering algorithms for iterative calculation. The detailed algorithms are given in Appendices A and B.

- To remain consistent with the actual operating state of the atomic clocks, the integrated algorithms in Appendix C are used. First, a long sliding-window ALGOS algorithm generates the ALGOS paper time of the constellation ensemble, and an LQG control algorithm periodically aligns the paper master-clock signal generated by weighted Kalman filtering to the ALGOS paper time. Second, the atomic-clock variances estimated by ALGOS are directly used as the Q matrix and weights of the weighted Kalman filter, thereby steering the parameters of the KPW algorithm.

At least one satellite in the constellation carries pulsar measurement equipment. Millisecond pulsars with high long-term stability are preferred. Pulsar time is used as the core calibration reference to correct the frequency of the constellation master clock.

- The satellite reference time-frequency is used as the reference. The arrival time of each X-ray pulse is measured, and corrections for time scale, space-time curvature, and optical-path geometry are applied to recover the observed pulsar time expressed in selenocentric coordinate time.

- The observed pulsar time is compared with the known timing model to obtain timing residuals.

- Wiener filtering is used to extract frequency offset from the residuals and to correct the frequency of the constellation master clock. The correction period T_p is closely related to the measurement accuracy of the pulsar equipment. For the same master-clock frequency accuracy index Δf, a higher measurement accuracy permits a shorter correction period:

$$T_p \geq \frac{\Delta\tau}{\Delta f}. \tag{10}$$

At least one satellite in the constellation carries equipment for comparison with Earth UTC. This equipment is used only to measure the time offset between the constellation paper master clock and Earth UTC. The measurement result does not participate in the generation or calibration of the paper master clock.

- A signal structure compatible with BeiDou global inter-satellite links is adopted.

- A same-frequency time-division measurement and communication link is established with BeiDou satellites for comparison with BDT. After correcting the BDT–UTC offset, the LST–UTC time offset is obtained.

- The same signal structure is used to establish an inter-satellite-type link with terrestrial equipment whose time-frequency is synchronized to UTC, thereby obtaining the LST–UTC time offset.

Lunar Standard Time (LST) is determined by its origin and scale. The origin is defined as the earliest epoch after stable operation of the constellation clock ensemble, aligned with the corresponding ground UTC epoch. The scale is defined by the frequency of the constellation paper master clock, reduced to selenocentric coordinate time.

Every satellite in the constellation computes the paper master clock and broadcasts it through inter-satellite links. The constellation randomly selects three satellites as primary computing nodes. Other satellites use the data from these three nodes and apply two-out-of-three voting to generate LSTF. Under nominal conditions, the paper master clocks of the three primary nodes remain consistent. If any node detects its own anomaly, it immediately exits the primary-node state. When other satellites detect that only two primary computing nodes remain, they immediately apply to become a primary node. The first applicant becomes the new primary node, ensuring that the constellation always contains three healthy primary computing nodes.

2.3 Space-Time Unification

According to relativistic space-time unification, the joint timekeeping laboratory formed by the lunar-orbit constellation requires corresponding accuracy for its own station positions. Conventional orbit determination of lunar-orbit satellites using Earth-based observation equipment has high routine maintenance cost and cannot satisfy the accuracy required for establishing standard time.

Precise orbit determination for lunar-orbit satellites should be completed in the lunar space-time frame, which is more consistent with the general physical setting. Otherwise, transformation errors between space-time frames and errors from Earth itself are inevitably introduced.

The lunar coordinate frame is defined by laser retroreflectors left by previous lunar landing missions. Although these reflectors are mainly distributed on the nearside for Earth observability, future lunar landing activities will place retroreflectors at more lunar locations.

By moving facilities equivalent to ground laser ranging equipment onto satellites, high-precision measurements of lunar-surface laser retroreflectors can be performed. With one coordinate fixed, joint estimation of the satellite orbit and the other retroreflectors can provide precise satellite orbits.

The current status of lunar laser retroreflectors is listed in Table 1.

The measured optical cross section (OCS) in the table is back-calculated from Earth laser ranging equipment under a 1064 nm wavelength, non-full-Moon conditions, long-term averaging, and normal incidence. Differences in latitude, lunar terrain, and illumination duration directly affect thermal distortion of the reflectors and the accumulation rate of lunar dust, leading to dispersion in the measured OCS values of the five reflector sets.

The laser measurement equation is

$$n_s = \frac{E_t}{hc/\lambda}\eta_t \frac{16}{\theta_t^2}\sigma \left(\frac{1}{4\pi r^2}\right)^2 A_r\eta_r\eta_Q. \tag{11}$$

Here, E_t is the single-pulse laser energy in joules, h is Planck's constant, λ is the laser wavelength in meters, η_t is the transmit efficiency, θ_t is the transmit beam divergence in radians, σ is the scattering cross section of the laser reflector in square meters, r is the link distance in meters, A_r is the effective receiving area in square meters, η_r is the receiving efficiency, and η_Q is the detector efficiency.

A 150 mm aperture laser measurement device is used onboard the satellite. With a transmitted pulse energy of 2×10^{-4} J, a pulse width of 80 ps, and a repetition frequency of 1000 Hz, the system measures laser retroreflectors at a distance of 10000 km. The received photon count is 2.1 photons per pulse, and the echo rate reaches 88%, enabling independent measurement of fixed lunar-surface references.

When the laser measurement accuracy is controlled within 10 mm, two days of measurements can determine the radial satellite orbit to 1 m. The resulting relativistic perturbation term is at the 10^{-18} level, satisfying the accuracy requirement for establishing lunar standard time.

2.4 Dissemination of Standard Time

The reference time-frequency of each satellite in the constellation is aligned to the constellation paper master clock.

A satellite whose inter-satellite-link transmit frequency is in the 2483–2500 MHz band is defined as state A. A state-A satellite broadcasts this signal to the lunar surface and lunar orbit using a wide lunar-coverage beam. It also receives user signals in the other two bands from the lunar surface and lunar orbit, thereby providing two-way time-frequency measurement services.

- The user modulates its own time-frequency information onto the f_b and f_c signals and transmits them to the state-A satellite.
- After recovering the user time-frequency information, the state-A satellite compares it with its onboard reference time-frequency and broadcasts the comparison result to the user through the f_a signal. The f_a signal also carries the satellite local reference time-frequency information.
- After recovering the reference time-frequency information of the state-A satellite, the user compares it with its own time-frequency and demodulates the data on the f_a signal to obtain the satellite-side comparison result.
- The user applies two-way satellite time and frequency transfer (TWSTFT) to calculate the time offset and frequency offset between the user and LSTF.
- User transmitted signals use frequency division plus code division to mitigate multi-user interference.

The state-A satellite also provides one-way time-frequency dissemination. Through the 2483–2500 MHz band, it broadcasts a spread-spectrum-code-modulated time-frequency signal to lunar-surface users and users at lunar-orbit altitude h. The user takes the received broadcast time minus the delay calculated by Eq. (12) as the reference

Table 1: Lunar laser retroreflectors in this study. Measured OCS ranges from 2006 to 2025.

Payload	Country	Latitude	Longitude	Ideal OCS (m^2)	Eng. OCS (m^2)	Measured OCS (m^2)
Apollo 11	USA	0.6734°N	23.4731°E	1.80×10^8	6.12×10^6	$(1.00 \sim 1.80) \times 10^7$
Apollo 14	USA	3.6442°S	17.4786°W	1.80×10^8	6.12×10^6	$(1.00 \sim 1.80) \times 10^7$
Apollo 15	USA	26.1334°N	3.6285°E	5.40×10^8	1.84×10^7	$(3.00 \sim 5.40) \times 10^7$
Lunokhod 1	USSR	38.3152°N	35.0080°W	9.00×10^7	3.06×10^6	$(0.50 \sim 1.00) \times 10^7$
Lunokhod 2	USSR	25.8323°N	30.9221°E	9.00×10^7	3.06×10^6	$(0.50 \sim 1.00) \times 10^7$

time. When $h \leq 200$ km, the reference-time accuracy is better than 10 μs:

$$d = \left[a_{sat}^2 + (R_m + h)^2 - 2a_{sat}(R_m + h) \times \cos\left(\frac{\pi}{2} - \arcsin\left(\frac{R_m + h}{a_{sat}}\right)\right)\right]^{1/2}, \tag{12}$$
$$\tau = \frac{d + a_{sat} - (R_m + h)}{2c}.$$

When a state-A satellite broadcasts in the 2483–2500 MHz band, spread-spectrum-code modulation is used. The spreading-code rate is 5.115 Mcps, the code period is 10230 chips, the information rate is 500 bps, and the frame length is 1000 bits.

3. Simulation and Analysis

For a lunar standard-time timekeeping laboratory composed of nine satellites in two orbital planes connected by inter-satellite links, it is assumed that each satellite carries two hydrogen clocks and one cesium clock. The three atomic clocks work simultaneously and perform pairwise phase comparison. At the same epoch, three phase-comparison measurements are available, with measurement accuracy not worse than 3 ps. One valid value per second is used for timekeeping. According to the frequency allocation, the nine satellites are divided into A, B, and C states. Links can be established between satellites in different states. At the same epoch, 27 inter-satellite comparison links are obtained. Through transfer of time-comparison data, each satellite is effectively able to establish measurement links with all other satellites within a one-hour period. The inter-satellite measurement accuracy is not worse than 15 ps, and one valid value every 3600 s is used for timekeeping.

In the simulation, the noise of each atomic clock is generated independently and scaled by the true variance factor of that clock. Hydrogen clocks have better short- and medium-term stability, while cesium clocks have larger noise parameters but better long-term stability. Phase is generated by integrating frequency. The frequency includes initial frequency offset, deterministic drift, white frequency noise, and random-walk frequency noise. One clock is also assumed to undergo a random 50 ns phase jump with an additional 3×10^{-13} frequency jump.

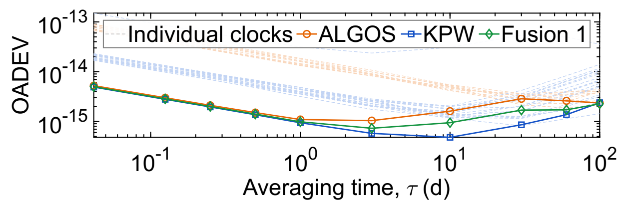

Fig. 3: Overlapping Allan deviation of atomic clocks and three paper-time algorithms under ideal conditions.

It is assumed that the true noise variance of each clock has an individual difference of $\pm 30\%$, and that the known prior variance of each atomic clock differs from the true value by no more than 10%.

KPW weights use the prior covariance of each atomic clock. Onboard filtering uses high-rate observations to estimate the phase and frequency of each clock relative to the local satellite reference. Inter-satellite filtering corrects slowly varying inter-satellite offsets once per hour. ALGOS does not directly weight the raw phase-comparison data; it acts on the Kalman predicted states. Its weights are determined only by the per-clock stability estimated from measured clock-difference data, without using any atomic-clock prior variance or KPW nominal covariance parameters. The weights are re-estimated every 30 days and smoothly transitioned over the following five days. When fusion algorithm 1 is used, LQG calibrates only the low-frequency offset of the KPW paper time and does not directly track the instantaneous phase noise of ALGOS.

For the lunar standard-time timekeeping laboratory, the KPW, ALGOS, and LQG-based ALGOS-steered KPW algorithms are used to generate paper time. Under absolutely ideal onboard and inter-satellite phase-comparison measurement conditions, with no measurement error, the ideal-state results are simulated and shown in Fig. 3.

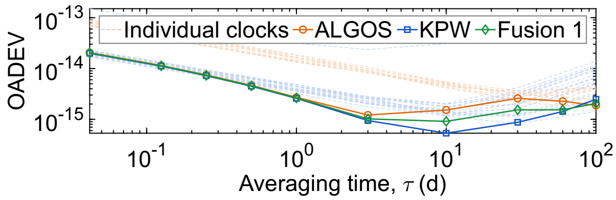

Fig. 4: Overlapping Allan deviation of atomic clocks and three paper-time algorithms under practical measurement conditions.

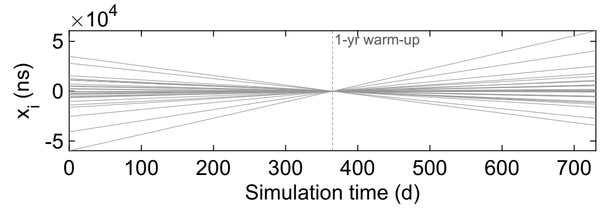

(a) Individual atomic clock offsets

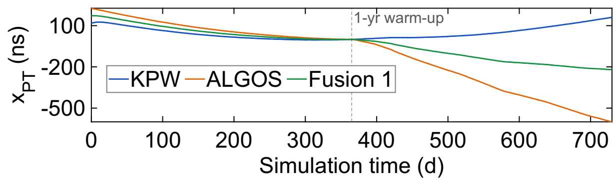

(b) Paper time offsets of three algorithms

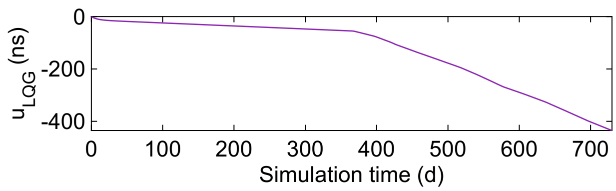

(c) LQG-based time corrections

Fig. 5: Time offsets of three paper-time algorithms and the control correction of fusion algorithm 1 under practical phase-comparison conditions.

Fig. 3 shows that, under ideal phase-comparison conditions, all three paper-time algorithms generally outperform a single atomic clock over averaging times from about one hour to ten days. ALGOS weights are estimated only from measured clock differences, and its OADEV values at one hour and one day are 5.2×10^{-15} and 1.1×10^{-15}, respectively. After ten days, random walk, drift, and finite-sample weight estimation gradually become the dominant error sources, reducing the gain from multi-clock combination.

Thus, KPW performs better in the short term when the prior variances are accurate. Pure measurement-based ALGOS does not use priors; after a one-year data window is formed, it can adjust per-clock weights according to actual stability and may outperform KPW at longer averaging times. The performance of fusion algorithm 1 depends on the long-term estimation quality of ALGOS and the LQG control bandwidth, and is not guaranteed to outperform both algorithms at all averaging times.

In practice, onboard and inter-satellite phase-comparison measurements both contain errors. When the onboard phase-comparison accuracy is not worse than 3 ps and the inter-satellite phase-comparison accuracy is not worse than 15 ps, the simulation is repeated. The results are shown in Fig. 4.

The phase-comparison link measurement noise mainly affects short-term stability. After adding 3 ps onboard noise and 15 ps inter-satellite noise, the OADEV of ALGOS is 2.1×10^{-14} at one hour and 2.7×10^{-15} at one day. As the averaging time increases, white measurement noise is gradually suppressed, but pure measurement-based weights remain affected by the finite sample of the one-year window, clock jumps, and long-term random walk.

Fig. 4 only shows the stability of paper time formed by multiple atomic clocks through onboard and inter-satellite phase-comparison measurements. The simulation results for the time offset of paper time are shown in Fig. 5.

Fig. 5 uses the paper time on day 365 as the zero point. After multiple Monte Carlo trials, the median one-year time-offset RMS values are 1044 ns for ALGOS, 853 ns for KPW, and 1116.0 ns for fusion algorithm 1. KPW has the smallest time-offset RMS when the prior variance is accurate. The effect of fusion algorithm 1 depends on the long-term estimation quality of ALGOS relative to KPW.

Each free-running atomic clock in orbit can be regarded as having good independence in its output frequency. However, because the number of clocks in the timekeeping ensemble is limited, the frequency distribution of all atomic clocks cannot fully exhibit Gaussian characteristics. Therefore, the time scale obtained by paper time has a certain offset from the true value.

In general, ground-test results for each atomic clock differ from its actual in-orbit stability to varying degrees. In this case, the true in-orbit characteristics of the 27 atomic clocks are kept identical to the preceding simulation, while only the ground-test priors held by the algorithms are changed: one third of the prior variances overestimate the in-orbit truth by half an order of magnitude, one third underestimate it by half an order of magnitude, and the remaining third differ from the in-orbit truth by no more than 10%. KPW uses these ground priors, while ALGOS weights are estimated only from measured clock differ-

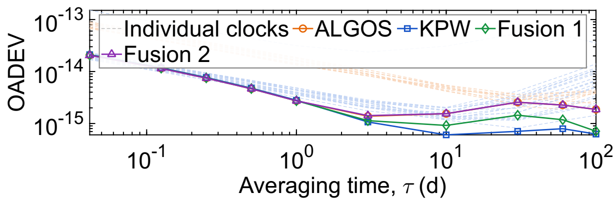

Fig. 6: Overlapping Allan deviation of four paper-time algorithms under clock-performance mismatch.

ences. The results of KPW, ALGOS, fusion algorithm 1, and fusion algorithm 2 are shown in Fig. 6.

Short-term stability is mainly determined by phase-comparison measurement noise. At one hour, the difference among the four algorithms is less than 3%. This indicates that near one hour, the common observation error formed by 3 ps onboard measurements and 15 ps inter-satellite measurements is larger than the difference among the weighting models. Changing the ground priors therefore does not significantly change the short-term frequency stability of paper time.

Medium- and long-term performance begins to be dominated by weights and clock-noise models. At ten days, the OADEV values of KPW, fusion algorithm 1, ALGOS, and fusion algorithm 2 are 6.0×10^{-16}, 9.2×10^{-16}, 1.5×10^{-15}, and 1.5×10^{-15}, respectively. At 30 days, the corresponding values are 7.1×10^{-16}, 1.4×10^{-15}, 2.6×10^{-15}, and 2.5×10^{-15}. KPW remains the best, indicating that large errors in ground priors do not necessarily degrade combination performance. Normalized weighting is more sensitive to whether the relative ranking of clock quality is wrong. In this clock-type and random-noise realization, the overestimated and underestimated groups may still assign larger weights to clocks that actually perform well.

Fusion algorithm 1 reflects a control-bandwidth trade-off. Its short-term result lies between ALGOS and KPW, and it partly retains the KPW advantage at the ten-day scale. However, its 30-day Monte Carlo median is higher than both, indicating that if LQG directly tracks the long-term frequency offset of ALGOS containing finite-sample fluctuations, it may inject low-frequency components caused by weight updates and clock jumps into KPW.

Fusion algorithm 2 is close to ALGOS. Both use per-clock variance estimated entirely from measured clock-difference data. The difference is that fusion algorithm 2 smooths weights and time increments through KPW-type recursion. Therefore, the two algorithms almost coincide in the short term, and the 30-day Monte Carlo results differ by only about 1.4%. If fusion algorithm 2 is to further outperform ALGOS, the Q-matrix update should distinguish white frequency noise, random walk, and drift components, rather than replacing all process-noise terms synchronously with a single total variance.

Overall, under 3 ps/15 ps measurement conditions, all four algorithms can form continuous paper time, but no single method dominates at all averaging times. It is recommended to use KPW prediction in the short term to suppress link noise, use pure measurement-based ALGOS in the medium and long term to correct prior ranking, and use a constrained low-bandwidth fusion mechanism for smooth switching. Ground-test priors should serve as KPW initialization and fault-recovery information, and should not enter ALGOS weight estimation.

After the international definition of lunar standard time is unified, relativistic corrections should be applied to the paper-time frequency before dissemination to users. During dissemination, the fused paper time must steer the physical time-frequency of each satellite timing signal in real time, ensuring that the second signal received by users is correct.

4. Conclusion

The proposed method focuses on the physical implementation of lunar standard time. Based on relativistic space-time unification, it establishes an independent standard time adapted to the lunar gravitational field and closely connected with the lunar coordinate frame. The method has the following characteristics.

First, time accuracy is significantly improved. The synchronization accuracy between Lunar Standard Time (LST) and BeiDou Time (BDT) is no worse than 0.5 ns, the synchronization accuracy with Earth UTC is no worse than 10 ns, the internal two-way synchronization accuracy on the lunar side is no worse than 0.2 ns, and the one-way broadcast synchronization accuracy is no worse than 10 μs. These values satisfy the needs of high-precision navigation, scientific experiments, and other missions.

Second, autonomy and controllability are strong. The system removes real-time dependence on Earth UTC and can independently maintain long-term stable LST operation during Earth–Moon link interruptions, supporting long-duration lunar habitation missions.

Third, stability is high. Through pulsar-time calibration and clock-difference compensation, the long-term frequency stability of LST is no worse than 1×10^{-15} per day, and the absolute time accuracy is better than 100 ns. The system is not affected by Earth rotation or UTC leap seconds.

Fourth, coverage is broad. The system supports fullscenario coverage of the lunar surface and near-lunar orbit, and is compatible with lunar bases, probes, rovers, and other user types.

Fifth, engineering feasibility is high. The system is based on mature onboard atomic clocks, onboard reference time-frequency technology, S-band inter-satellite links, BeiDou inter-satellite-link technology, time-frequency signal generation and dissemination technology, and deep-space tracking, telemetry, and command technology. Combined with lunar-environment adaptation, the technology readiness is high and the system is easy to implement.

Sixth, scalability is strong. The constellation architecture supports expansion in the number of satellites, and the method can be adapted to future deep-space exploration, Mars resource development, and other new mission requirements.

References

[1] A Bourgoin, P Defraigne, and F Meynadier. Lunar reference timescale. *Metrologia*, 63(1):015003, jan 2026.

[2] Neil Ashby and Bijunath R. Patla. A Relativistic Framework to Estimate Clock Rates on the Moon. *The Astronomical Journal*, 168(3):112, aug 2024.

[3] E.J. Öpik. The lunar atmosphere. *Planetary and Space Science*, 9(5):211–244, 1962.

[4] J.S. Halekas, Y. Saito, G.T. Delory, and W.M. Farrell. New views of the lunar plasma environment. *Planetary and Space Science*, 59(14):1681–1694, 2011. Lunar Dust, Atmosphere and Plasma: The Next Steps.

[5] Paul Lucey, Randy L. Korotev, Jeffrey J. Gillis, Larry A. Taylor, David Lawrence, Bruce A. Campbell, Rick Elphic, Bill Feldman, Lon L. Hood, Donald Hunten, Michael Mendillo, Sarah Noble, James J. Papike, Robert C. Reedy, Stefanie Lawson, Tom Prettyman, Olivier Gasnault, and Sylvestre Maurice. Understanding the Lunar Surface and Space-Moon Interactions. *Reviews in Mineralogy and Geochemistry*, 60(1):83–219, 01 2006.

[6] S. Alan Stern. The lunar atmosphere: History, status, current problems, and context. *Reviews of Geophysics*, 37(4):453–491, 1999.

[7] J.-P. Williams, B. T. Greenhagen, D. A. Paige, N. Schorghofer, E. Sefton-Nash, P. O. Hayne, P. G. Lucey, M. A. Siegler, and K. Michael Aye. Seasonal Polar Temperatures on the Moon. *Journal of Geophysical Research: Planets*, 124(10):2505–2521, 2019.

[8] Steve Creech, John Guidi, and Darcy Elburn. Artemis: An Overview of NASA's Activities to Return Humans to the Moon. In *2022 IEEE Aerospace Conference (AERO)*, pages 1–7, 2022.

[9] Marshall Smith, Douglas Craig, Nicole Herrmann, Erin Mahoney, Jonathan Krezel, Nate McIntyre, and Kandyce Goodliff. The Artemis Program: An Overview of NASA's Activities to Return Humans to the Moon. In *2020 IEEE Aerospace Conference*, pages 1–10, 2020.

[10] Pietro Giordano, Floor Malman, Richard Swinden, Paolo Zoccarato, and Javier Ventura-Traveset. The Lunar Pathfinder PNT Experiment and Moonlight Navigation Service: The Future of Lunar Position, Navigation and Timing. In *Proceedings of the 2022 International Technical Meeting of the Institute of Navigation*, pages 632–642, Long Beach, California, January 2022. Institute of Navigation.

[11] Zhaoyu Pei, Jizhong Liu, Qian Wang, Yan Kang, Yongliao Zou, He Zhang, Yuhua Zhang, Huaiyu He, Qiong Wang, Ruihong Yang, Wei Wang, and Jinan Ma. Overview of Lunar Exploration and the International Lunar Research Station. *Chinese Science Bulletin*, 65(24):2577–2586, 2020.

[12] Teng Hu, Ze Yang, Mo Li, Carolyn H. van der Bogert, Zhizhong Kang, Xiaojian Xu, and Harald Hiesinger. Possible sites for a chinese international lunar research station in the lunar south polar region. *Planetary and Space Science*, 227:105623, 2023.

[13] T. M. Eubanks, J. W. Blase, S. Asmar, and B. G. Bills. Modeling Lunar Time. In *LPI Contributions*, volume 3063 of *LPI Contributions*, page 5025, October 2024.

[14] Serena Molli, Agnès Fienga, Pascale Defraigne, Krzysztof Sośnica, Luigi Cacciapuoti, Luca Porcelli, Lotfi Massarweh, Sara Bruni, Riccardo Pozzobon, Albert Roura, Francesco Vespe, Diego Blas, Ozgur Karatekin, Yoann Audet, Floor Melman, Richard Swinden, Javier Ventura-Traveset, Olivier Alibart, Marie-Christine Angonin, Daniel Arnold, Ruth Bamford, Emmanuele Battista, Marco Belloni, J. C. Berton, Orfeu Bertolami, Mathis Bloßfeld, Adrien Bourgoin, Giada Bargiacchi, Salvatore Buoninfante, Nicolò Burzillà, Roberto Campagnola, Paolo Cappuccio, Salvatore Capozziello, Giuseppe Cimò, Clément Courde, Rolf Dach, Mario Siciliani de Cumis, Simone Dell'Agnello, Fabrizio De Marchi, Valentina Galluzzi, Francesco Gini, Philipp Glaeser, Klaus

Gwinner, Alex Guinard, Rüdiger Haas, Aurélien Hees, Hauke Hussmann, Luciano Iess, Alexander C. Jenkins, Siddarth K. Joshi, Maria Karbon, Sergei Klioner, Kaisa Laiho, Christophe Le Poncin-Lafitte, Marco Lucente, David Lucchesi, Riccardo March, Lucia McCallum, Jürgen Müller, Weijie Nie, Jillian Oduber, Roberto Peron, Francesco Picciariello, Théo Pichavant, Michael Plumaris, Eleonora Polini, Ana-Catalina Plesa, Dimitrios Psychas, Bernardino Quaranta, Nicolas Rambaux, Marc Rovira-Navarro, Francesco Santoli, Matthias Schartner, Florian Seitz, Ilaria Sesia, Yan Seyffert, Stefano Speretta, Tim Springer, Giuseppe Vallone, Paolo Villoresi, Sebastien Vincent-Bonnieu, Ben Wadsworth, Pierre Waller, Radosław Zajdel, and Erik Schoenemann. NovaMoon: A Strategic Lunar Reference Station for Positioning, Timing, and Largely Enhanced Science in the Earth-Moon System, 2026.

[15] Min Liu, Hezhen Yu, Hongbo Jin, Jinsong Ping, Wenxiao Li, Yongjun Wang, Zhoujian Cao, Wenzhao Zhang, Mingxue Shao, Jie Yang, and Jianguo Yan. The Rule of Time Outside the Earth: Timekeeping and Time Service on the Moon. *Scientia Sinica Physica, Mechanica & Astronomica*, 56(3):239512, 2026.

[16] Shaojun Bi, Changgang Zheng, Congwei Yang, Jinjun Zheng, Chengyan He, and Jiaxing Liu. In-orbit Experimental of Satellite-induced Code Pseudorange Deviations of BeiDou System. In *Proceedings of the 31st International Technical Meeting of the Satellite Division of the Institute of Navigation (ION GNSS+ 2018)*, pages 1257–1267, Miami, Florida, USA, September 2018. Institute of Navigation.

[17] Huan Yan, Juan A. Fraire, Ziqi Yang, Kanglian Zhao, Wenfeng Li, Jinjun Zheng, Ziyu Wang, and Changgang Zheng. Progressive Replacement Sequence Planning for Laser-Enhanced BeiDou Navigation Constellations, 2026.

[18] Yiwei Wu and Siran Liu. Determination of mathematical expectations of two weighting statistics for ensemble time scales. *Metrologia*, 60(6):065009, oct 2023.

[19] Patrizia Tavella and Claudine Thomas. Time Scale Algorithm: Definition of Ensemble Time and Possible Uses of the Kalman Filter. In *Proceedings of the 22nd Annual Precise Time and Time Interval Systems and Applications Meeting*, pages 157–170, Vienna, VA, USA, December 1990.

[20] Qiang Li, Ranyang Li, Kaifan Ji, and Wei Dai. Kalman Filter and Its Application. In *2015 8th International Conference on Intelligent Networks and Intelligent Systems (ICINIS)*, pages 74–77, 2015.

Appendix A. ALGOS Algorithm

Let $EAL_{ALGOS}(t)$ be the ensemble atomic time:

$$EAL_{ALGOS}(t) = \sum_{i=1}^{N} w_i x_i(t). \tag{A.1}$$

Here, $x_i(t)$ is the time of the ith atomic clock, and w_i is the weight of the ith atomic clock. Define $\tau_i(t)$ as the offset between the ith atomic clock and the ensemble atomic time:

$$\tau_i(t) = EAL_{ALGOS}(t) - x_i(t). \tag{A.2}$$

Let $x_i^j(t)$ be the phase-comparison data between the ith and jth atomic clocks:

$$x_j(t) - x_i(t) = \tau_i(t) - \tau_j(t) = x_i^j(t), \quad i, j = 1, 2, \ldots, N. \tag{A.3}$$

Let $h_i'(t)$ be the predicted value of $\tau_i(t)$. Then

$$\begin{aligned} \tau_j(t) &= \sum_{i=1}^{N} w_i [\tau_i(t) - x_i^j(t)] \\ &= \sum_{i=1}^{N} w_i [h_i'(t) - x_i^j(t)], \quad j = 1, 2, \ldots, N. \end{aligned} \tag{A.4}$$

The weight of the ith atomic clock is

$$w_i = \frac{1/\sigma_{\varepsilon_i}^2}{\sum_{j=1}^{N}(1/\sigma_{\varepsilon_j}^2)}, \quad i = 1, 2, \ldots, N, \tag{A.5}$$

where $\sigma_{\varepsilon_i}^2$ is the Allan variance of the ith atomic clock.

The predicted value $h_i'(t)$ of $\tau_j(t)$ is obtained from the phase offset, frequency offset, and frequency-drift offset between the ith atomic clock and the ensemble atomic time at epoch t_k:

$$h_i'(t) = \tau_i(t_k) + A(t_k)(t - t_k) + 0.5B(t_k)(t - t_k)^2. \tag{A.6}$$

Here, $A(t_k)$ is the mean frequency offset, which may be fitted from 12 samples of $A(t_k)$, and $B(t_k)$ is the mean frequency-drift offset, which may be fitted from six samples of $B(t_k)$:

$$A(t_k) = \frac{\tau_i(t_k) - \tau_i(t_{k-1})}{T_A}, \quad B(t_k) = \frac{A(t_k) - A(t_{k-1})}{T_B}. \tag{A.7}$$

In general, one month of time-comparison data is used to estimate the frequency offset relative to EAL, and six months of frequency-offset data are used to compute the frequency stability relative to EAL. The weights are updated once per month:

$$\sigma^2_{\varepsilon_i}(\tau) = \frac{1}{2(M-1)} \sum_{k=1}^{M-1} \left[A_i(t_{k+1}) - A_i(t_k)\right]^2 . \quad \text{(A.8)}$$

The weight parameters of each atomic clock may also be dynamically adjusted by computing the double-overlapping two-sample variance:

$$\sigma^2_{\varepsilon_i}(\tau) = \frac{1}{2(M-2)} \sum_{k=1}^{M-2} \left[x_i(t_{k+2}) - 2x_i(t_{k+1}) + x_i(t_k)\right]^2 . \quad \text{(A.9)}$$

Appendix B. KPW Algorithm

The state equation is

$$X_{k+1} = \Phi X_k + q_k. \quad \text{(B.1)}$$

Here, X_k is the time and frequency vector of the atomic clocks in the ensemble, and q_k is the corresponding noise vector:

$$X_k = [x_1(k)\ y_1(k)\ \cdots\ x_N(k)\ y_N(k)]^T, \quad \text{(B.2)}$$

$$q_k = [\varepsilon_1(k)\ \eta_1(k)\ \cdots\ \varepsilon_N(k)\ \eta_N(k)]^T. \quad \text{(B.3)}$$

Φ is the state-transition matrix, and Q_k is the atomic-clock time-variance and frequency-variance matrix.

$$\begin{aligned} \Phi &= \mathrm{blkdiag}\left(\begin{bmatrix}1 & T\\ 0 & 1\end{bmatrix}, \ldots, \begin{bmatrix}1 & T\\ 0 & 1\end{bmatrix}\right), \\ Q_k &= \mathrm{blkdiag}\left(\begin{bmatrix}\sigma^2_{\varepsilon_1} & 0\\ 0 & \sigma^2_{\eta_1}\end{bmatrix}, \ldots, \begin{bmatrix}\sigma^2_{\varepsilon_N} & 0\\ 0 & \sigma^2_{\eta_N}\end{bmatrix}\right). \end{aligned} \quad \text{(B.4)}$$

Let Z_k be the measurable atomic-clock phase-comparison vector, and let V be the phase-comparison measurement-noise vector:

$$\begin{aligned} Z_k &= [x_1(k) - x_2(k)\ x_1(k) - x_3(k)\ \cdots\ x_1(k) - x_N(k)]^T, \\ V &= [v_1\ v_2\ \cdots\ v_{N-1}]^T. \end{aligned} \quad \text{(B.5)}$$

Then

$$Z_k = HX_k + V. \quad \text{(B.6)}$$

The observation matrix H and covariance matrix R_k are the corresponding phase-comparison matrices.

The Kalman recursion is

$$X_{k,k-1} = \Phi_{k,k-1} X_{k-1}, \quad \text{(B.7)}$$

$$P_{k,k-1} = \Phi_{k,k-1} P_{k-1} \Phi^T_{k,k-1} + Q_{k-1}, \quad \text{(B.8)}$$

$$K_k = P_{k,k-1} H_k^T (H_k P_{k,k-1} H_k^T + R_k)^{-1}, \quad \text{(B.9)}$$

$$X_k = X_{k,k-1} + K_k(Z_k - H_k X_{k,k-1}), \quad \text{(B.10)}$$

$$P_k = (I - K_k H_k) P_{k,k-1}. \quad \text{(B.11)}$$

The frequency of each atomic clock is updated by the equations above, while the time update for the KPW paper atomic clock is

$$x_j = \sum_{i=1}^{N} w_i(t) \left[x_j^i(k) + x^i(k-1) + T_A y^i(k-1)\right] . \quad \text{(B.12)}$$

Here, $x_j^i(k) = x_j(k) - x_i(k)$, and $w_i(t)$ is calculated from the prior variance of the atomic clocks.

Appendix C. Fusion Algorithms

Algorithm 1 uses KPW to calculate the time and frequency of each atomic clock and form KPW paper time. The ALGOS paper time calculated by ALGOS is then used to steer KPW paper time on large time scales. This exploits the ability of ALGOS to estimate atomic-clock variance in real time from a larger set of measurement data, producing weights that better match the actual operating state of the clocks. LQG steering of paper time should ensure smooth and continuous phase.

Algorithm 2 does not use prior data for the atomic-clock time-variance and frequency-variance matrix Q_k in KPW. Instead, it uses variances estimated by ALGOS from the actual operating state, adapting to performance changes during atomic-clock operation.